

Thermoelectric transport properties of PbTe under pressure

Lanqing Xu (徐兰青)

Department of Physics, Institute of Theoretical Physics and Astrophysics, and Fujian Key Laboratory of Semiconductor Materials and Applications, Xiamen University, Xiamen 361005, People's Republic of China and Key Laboratory of OptoElectronic Science and Technology for Medicine of Ministry of Education, Fujian Normal University, Fuzhou 350007, People's Republic of China

Yongping Zheng (郑勇平)

School of Physics and OptoElectronics Technology, Fujian Normal University, Fuzhou 350007, People's Republic of China

Jin-Cheng Zheng (郑金成)*

Department of Physics, Institute of Theoretical Physics and Astrophysics, and Fujian Key Laboratory of Semiconductor Materials and Applications, Xiamen University, Xiamen 361005, People's Republic of China

(Received 10 May 2010; revised manuscript received 8 October 2010; published 2 November 2010)

In this work, we present a comprehensive picture of structural, dynamical, electronic, and transport properties of PbTe at ambient and high pressures. The first-principles linear-response calculations show that there exists an anharmonic instability of the optical branch phonon at the Brillouin-zone (BZ) center and soft phonons at the BZ boundary X point. The k -dependent soft modes may lead to substantial changes in the thermal conductivity when the pressure is applied. The electronic band structure of both $B1$ and $Pnma$ phases are investigated by full potential method with various exchange-correlation functionals. Under pressure there is a band-gap closure as well as reopening within $B1$ structure whereas for $Pnma$ phase only the gap closure is observed. Their thermoelectric transport properties are studied by exploring their energy bands based on Boltzmann transport theory. We found that n -doped $Pnma$ phase at 6.7 GPa has better thermoelectric performance than $B1$ phase at ambient condition, while for the p -doped case, $B1$ phase has much better thermoelectric properties. Energy band gap does play an important role in thermoelectric performance. At 300 K, modifications of thermoelectric properties caused by band-gap variation can be observed only at a low doping level, at 600 K the influence can be detected in mid-to-high doping levels. The detailed analysis of thermoelectric properties as respect to temperatures and carrier concentrations reveal that in the low-doping case the optimal performance occurs in 300–450 K temperature range but for mid-to-high doping cases the optimal working temperature increase to higher range. With the pressure applied, the thermoelectric response shows many interesting features. The thermoelectric figure of merit (ZT) for $B1$ phase achieves its maximum at middoping region with ~ 8 GPa for p doping and above 18 GPa for n doping. In the $Pnma$ case, ZT values are more sensitive to doping than to pressure, and there is small difference between the 300 and 600 K results. These findings are expected to be useful in searching an optimal combination of doping level, working temperature, and pressure in order to achieve higher ZT in PbTe-based materials.

DOI: [10.1103/PhysRevB.82.195102](https://doi.org/10.1103/PhysRevB.82.195102)

PACS number(s): 72.20.Pa, 71.20.Nr, 63.20.D–

I. INTRODUCTION

Developing efficient thermoelectric (TE) semiconductors has never lost their attraction over the past several decades due to their promising performances in the energy conversion applications.^{1–3} Lead telluride (PbTe) based alloys are known as appropriate candidates for n -type legs in midtemperature TE devices owing to its narrow band gap, large average exciton Bohr radius (~ 46 nm) and low thermal conductivity which is unusual for materials with simple structure.⁴ PbTe is crystallized in a small, high-symmetry unit cell with sixfold coordination of both atomic species. The n -type PbTe has low thermal conductivity and relative high values of thermoelectric figure of merit above room temperature. Currently it is still one of the best commercial bulk TE materials for solid-state energy conversion at operating temperature between 400 and 800 K.⁵

The thermal-to-electricity conversion efficiency of a TE material is evaluated in terms of a dimensionless figure of merit $ZT = (S^2\sigma T / \kappa)$, where T is absolute temperature, S is

the thermoelectric power, namely, Seebeck coefficient, σ is electrical conductivity, κ is thermal conductivity, respectively.³ The electronic quantities are combined to give $S^2\sigma$, which is the so-called *power factor* and can be optimized by varying the carrier concentration of the material. The thermal conductivity contains electronic component κ_e and lattice component κ_l . κ_e is determined by the detailed band structure and the carrier concentration and κ_l is controlled by the bond strength and crystal structure of the material. High-quality TE materials should therefore have large power factor and low thermal conductivity. Various means have been proposed to guide the search for high ZT thermoelectric materials. Traditionally they include increasing power factor by doping to adjust the carrier concentrations or by using quantum effect; or synthesizing of new materials; or lowering thermal conductivity by disordered structures, or using quantum effect or materials with complex superlattice, or nanoeffects.⁶ In 1996, Harman *et al.*⁷ synthesized PbTe/Pb_{1-x}Eu_xTe multiple quantum-well samples with $ZT > 1.2$, which is a result breaking the decades-record ZT

$\cong 1.0$ barrier for the TE materials at 300 K. In 2005, Caylor *et al.*⁸ reported a PbTe/PbTe_{0.75}Se_{0.25} superlattice structure which is believed to enhance the TE performance by reducing lattice thermal conductivity down to ~ 5 mW/cm K. In what follows, Tai *et al.*⁹ synthesized single-crystalline pearl-necklace-shaped PbTe nanowires with a Seebeck coefficient of $307 \mu\text{V/K}$, higher than $265 \mu\text{V/K}$ of the bulk samples. In 2009, Wan *et al.*⁴ reported a lead telluride film nanorod sample with a large Seebeck coefficient of $679.8 \mu\text{V/K}$ at room temperature, which is about 2.56 times larger than that of bulk material. More recently, the LAST-*m* compounds AgPb_{*m*}SbTe_{*m+2*} have arisen as another attractive alloy with *ZT* value well above unity.^{10,11}

Pressure tuning may also offer another effective method to enhance TE properties. At present the exploration of intermediate high-pressure phase of materials with high TE performance is becoming an active research field. The effect of pressure on the phase transition of HgTe and accompanied changes in thermopower has been studied nearly half a century ago;¹² recently Chen *et al.* predicted its cinnabar phase to be a good TE material.¹³ Li *et al.*¹⁴ studied the effects of pressure on the dynamical, electronic, and transport properties of AuX₂ (*X*=Al, Ga, and In), and found that pressure influenced the band structure close to the Fermi surface and caused changes in the transport properties. In 2007, Zhuravlev found the energy band gap of PbSe and CdSe have a decreasing trend with pressure.¹⁵ In what follows, Streltsov *et al.*¹⁶ measured the crystal lattice and band structure of the intermediate high-pressure phase of PbSe; the obtained thermopower and resistivity have a remarkable change with pressure applied. The corresponding TE results suggest the intermediate phase to be the *Pnma* type. Among the IV-VI compounds, the effect of pressure on the phase transition of PbTe has been documented since 1967 (Ref. 17) and recently Wang *et al.*¹⁸ found its high-pressure intermediate *Pnma* phase possesses enhanced TE performance than the *B1* phase. PbTe crystallizes at room temperature in cubic NaCl structure (*B1*) with *Fm3m* space group, which is stable under midtemperature to high temperature but unstable when pressure is applied. At the pressure of ~ 6 GPa, this compound undergoes a reversible phase transition from cubic to orthorhombic symmetry which is only recently been clarified to be *Pnma* space group.^{19,20} This is an intermediate phase distorted from the NaCl structure which is doubled along $[\bar{1}10]$ direction and the major atomic displacements are along $[001]$ direction of the cubic structure. At pressure above ~ 13 GPa, this structure begins a second phase transition to the CsCl-type (*B2*) lattice and finishes at ~ 16 GPa.^{6,20} For the effect of pressure on the thermoelectric properties for PbTe, Ovsyannikov *et al.*²¹ mentioned the band-gap closure in the $[B1 \rightarrow B2]$ phase transition; An *et al.*²² analyzed the phonon dispersions under pressure and found *k*-dependent soft modes which may be the secret ingredient for its low thermal conductivity. Colossal pressure-tuned improvement of TE efficiencies was also discovered for PbTe-based crystals under pressure of 2–3 GPa.²³ Large improvements in the TE properties of PbTe synthesized under high-temperature and high-pressure circumstance has also been documented.²⁴ Moreover, McGuire *et al.*²⁵ reported a reversible change in TE

properties by high-temperature high-pressure treatment of conventionally synthesized PbTe samples.

It can be seen that carrier concentration, working temperature, and pressure all influence the *ZT* values of PbTe. However, there is no report so far on how to optimize these factors to improve its TE performance. In this work we perform *ab initio* calculations to determine ground state and dynamical properties such as phonon dispersions and use the obtained results to analyze pressure-induced atomic structure change for PbTe in $[B1 \rightarrow Pnma]$ phase transition. A further first-principles calculation using the full-potential linearized augmented plane-wave method (FP-LAPW) (Ref. 26) is carried out to study the electronic band structures and Boltzmann transport theory^{27,28} is used to derive the thermoelectric properties. We then propose several ways for optimizing thermoelectric properties of PbTe in terms of carrier concentration, temperature, and pressure.

II. COMPUTATION METHOD

We carry out first-principles calculations using both plane waves and norm-conserving pseudopotentials (PW-PPs) as implemented in the ABINIT program package,²⁹ as well as FP-LAPW method, as implemented in the WIEN2K code²⁶ within the framework of density-functional theory (DFT).³⁰ In the ground-state calculations, the exchange-correlation (XC) effects was evaluated using both local-density approximation (LDA) and generalized gradient approximation (GGA) with and without the consideration of spin-orbital (SO) coupling effect. In the lattice dynamical calculation, properties were investigated using the density-functional perturbation theory.^{31,32} Hartwigsen-Goedecker-Hutter pseudopotentials³³ with an energy cutoff of 45 hartree were used and the Brillouin-zone summation was performed on a $8 \times 8 \times 8$ Monkhorst-Pack grid.³⁴ In the ground-state calculations, the lattice parameters were optimized through minimization of the total energy while in the band structure and transport calculation the lattice constants were set to the experimental values, i.e., 6.46 \AA (Ref. 35) for *B1* phase and ($a=8.157 \text{ \AA}$, $b=4.492 \text{ \AA}$, $c=6.294 \text{ \AA}$) (Ref. 20) for *Pnma* phase.

The electronic band structures and density of states (DOS) calculations were calculated using all-electron method. SO interactions were included here to account for the relativistic effect due to the large atomic mass of Pb. The muffin-tin radii were chosen to be 2.5 a.u. for both Pb and Te. The plane-wave cutoff was defined by $R_{\text{MT}} * K_{\text{max}} = 10$, which gives good convergence. Eigenenergies were calculated using a nonshifted mesh with 56 000 *k* points. The Perdew-Burke-Ernzerhof (PBE) GGA (Ref. 36) approximation was employed in the band-structure calculations. It is well known that most DFT-based functionals yield poor band gaps and this will induce large deviation in the calculation of thermoelectric properties.³⁷ In the transport calculation, the band gap was corrected using experimental values and Engel-Vosko (EV) GGA (Ref. 38) results, which will be discussed in Sec. III D.

The Boltzmann transport equation and constant relaxation-time approximation were used to calculate trans-

port properties as implemented in the BOLTZTRAP code.^{28,37} With this assumption, the Seebeck coefficient S , the electrical conductivity relative to relaxation time σ/τ can be calculated without any fitting parameter. The electrical conductivity σ , hence the power factor $S^2\sigma$ and ZT values, can however only be resolved with respect to τ . In narrow band-gap semiconductors such as lead chalcogenides, the energy region of interest as measured from the band edge is comparable to the band gap E_g . To get a quantitative analysis of electrical conductivity and figure of merit, we used nonparabolic Kane model to describe the dependence of energy on crystal momentum and applied this model to treat τ . It was found in the previous studies³⁹ that the dominant scattering mechanisms are by point defects and thermal phonons and the main contributions to the relaxation time at temperatures above 300 K come from acoustic-phonon deformation potential τ_a , optical-phonon deformation potential τ_o and polar scattering by optical phonon τ_{po} . Therefore, we consider only these three parts and get

$$\tau = (\tau_a^{-1} + \tau_o^{-1} + \tau_{po}^{-1})^{-1}. \quad (1)$$

Details about $\tau_a, \tau_o, \tau_{po}$ can be found in Refs. 39 and 40. With given τ , ZT can be evaluated by

$$ZT = \frac{S^2\sigma T}{\kappa_e + \kappa_l} = \frac{S^2}{L_0 + \frac{\kappa_l}{\sigma T}}, \quad (2)$$

where L_0 is the Lorentz number. In order to compare calculated TE properties such as σ/τ , $S^2\sigma/\tau$, and ZT with experimental data, the relaxation time τ obtained by Eq. (1) is used, as discussed in following sections and presented in Figs. 9–11, and Figs. 13–15. While in Fig. 12, a constant τ is used for simplification.

III. RESULTS AND DISCUSSION

A. Ground-state properties of PbTe

We first calculated the ground-state properties of bulk PbTe in $B1$ and $Pnma$ phases. Results from different methods (pseudopotential and all electron) and different XC functionals (LDAs and GGAs) are listed in Table I and compared with previously reported DFT values, as well as experimental data. The theoretical total energies as a function of volume are evaluated and fitted to the Murnaghan⁴¹ equation of state to obtain the theoretical equilibrium lattice parameter, bulk modulus, and the pressure derivative of bulk modulus. Compared with the measured lattice constants, those calculated by LDA are about 1.7% smaller and those by GGA are about 1.8% larger. This is consistent with the fact that LDA usually underestimates while GGA overestimates unit-cell volume.⁴²

Hardness is one of the most important issues in the study of the ground-state properties.^{43,44} The all-electron relativistic PBE-GGA calculation predicts a bulk modulus value of 38.5 GPa for $B1$ phase, in good agreement with experimental measurement 40–41.1 GPa.⁴⁵ The bulk modulus of the orthorhombic structure is about ~ 40 GPa from GGA calculation, which is slightly larger than that of cubic instance. It is found

that the bulk modulus is not sensitive to SO coupling.

B. Lattice dynamics of PbTe under pressure

Lattice dynamics plays an important role in understanding the micro mechanisms of phase transitions. In the case of $[\text{NaCl} \rightarrow \text{orthorhombic} \rightarrow \text{CsCl}]$ phase transition the doubly degenerated transverse acoustic (TA) mode in the high-symmetry NaCl structure is softened and may lead to freezing phonon amplitude at X point. In order to make a further check on the stability of the NaCl structure, we calculated phonon frequencies at the BZ boundary X point for pressures up to 20 GPa, as shown in Fig. 1. The TA phonons adopt a parabolic decreased trend with increasing pressure. At ~ 18.5 GPa, a TA phonon branch drops to zero frequency. The critical pressure here is comparable to the experimental value of 16 GPa which is needed for the second transition $[\text{Pnma} \rightarrow \text{B2}(\text{CsCl})]$.²⁰ This mode-softening behavior at X point should be related to the particular mechanism that is responsible for the $[B1 \rightarrow B2]$ phase transition.

Lead chalcogenides possess zone-center transverse optical (TO) phonon instability, which is an inversion center breaking phonon, and would lead to a ferroelectric ground state if it were actually unstable.²² SnTe and GeTe are ferroelectric materials with rhombohedral ground state. Although PbTe crystallizes in NaCl ground state, it may also be liable to ferroelectricity, as can be seen from Fig. 2. The frequencies of the longitudinal optical (LO) and doubly degenerate TO modes at Γ point are plotted as a function of pressure. One observes that with increasing pressure, the TO and LO modes move to higher frequencies, there is a strong pressure dependence of the TO modes. Strong pressure dependence means strong volume dependence. From the phonon dispersions in Fig. 3(a) it is clear that there is a strong coupling between TO and LA/TA branches. The strong volume dependence in Fig. 2 indicates large anharmonic coupling between the TO and TA phonons. The softening of acoustic phonon (Fig. 1) and large anharmonic coupling between acoustic and optical phonons under pressure suggests reduced thermal conductivity because normally heat is mainly carried by acoustic phonons in materials, especially at high temperature, as we studied here. Our calculations (not shown) confirm that even small local strain variation can cause observable shift of the acoustic part of phonon DOS to lower frequency region, from this aspect reduced thermal conductivity is expected. However, the optical phonons stiffen under pressure, one might suppose this corresponds to increasing thermal conductivity. Therefore, the total thermal conductivity is a result of the competition between the pressure-induced modification of low-frequency and high-frequency phonons. For thermoelectric properties, the anharmonicity could lead to increased phonon scattering when temperature goes high. This could partly explain the low thermal conductivity of this material with high-symmetry simple structure.

C. Electronic band structures and density of states

An accurate energy band structure is essential in obtaining reliable transport properties. Calculated band gaps from various combinations of computational methods are listed in

TABLE I. The theoretical lattice constants, energy band gap, bulk moduli, and pressure derivative of bulk moduli for PbTe crystallizes in $B1$ and $Pnma$ phases. Results are compared with previously reported computation values and available experiment data. In the PW-PP calculation, band gaps were obtained using experimental lattice constant; in the FP-LAPW situation band gaps for both equilibrium and experimental lattice constants were calculated.

		a_0 (Å)	E_g (eV)	B_0 (GPa)	B'
<i>B1</i> phase					
		This work			
PW-PP	LDA	6.35	0.64 ^a	46.0	4.27
	LDA+SO	6.34	0.18 ^a	46.0	4.53
	GGA-PBE	6.56	0.70 ^a	37.0	4.61
	GGA-PBE+SO	6.55	0.11 ^a	38.5	4.53
FP-LAPW	PBE-GGA+SO	6.58	0.08 ^a	38.5	4.50
			0.22 ^b		
	EV-GGA+SO		0.20 ^a		
		Literature			
LMTO	LDA ^c	6.34			
FP-LAPW	GGA+SO ^d	6.57	0.16	39.4	3.92
		Experiment			
		6.46 ^e	0.19 ^f		
			0.31 ^g	41.1 ^h	
<i>Pnma</i> phase					
		This work			
PW-PP	LDA	8.36	0.26 ^a	49.7	4.34
	LDA+SO	8.32		48.3	4.41
	GGA-PBE	8.58	0.32 ^a	40.0	4.73
	GGA-PBE+SO	8.61		38.3	4.84
FP-LAPW	PBE-GGA+SO	8.61	0.11 ^a	40.3	4.57
			0.21 ^b		
	EV-GGA+SO		0.22 ^a		
		Experiment			
		$a=8.157$ ⁱ	0.355 ^j		
		$b=4.492$ ⁱ	0.420 ^k		
		$c=6.294$ ⁱ			

^aBand gap calculated at experimental lattice constant.

^bBand gap calculated at equilibrium lattice constant.

^cReference 68.

^dReference 47.

^eReference 35.

^fReference 46 at 4 K.

^gReference 46 at 300 K.

^hReference 45 at 300 K.

ⁱReference 20 at 6.7 GPa.

^jReference 48, thin film at 77 K.

^kReference 48, thin film at 320 K.

Table I, among which only the band structures from FP-LAPW PBE-GGA+SO calculation are shown in Fig. 4. PW-PP method without including SO coupling gives rather large deviation in predicting the band gap, which further confirms that SO effect plays an important role in the energy band structure and cannot be omitted. SO coupling lowers

the system's symmetry; causes level repulsion between equal symmetry states; pushes them up or down; splits bands and alters the band gap. Relativistic terms become important for heavy elements such as in this case of Pb cation. The calculated results including the SO effect show these behaviors. In $B1$ situation, the Pb 6s band possesses the same symmetry as

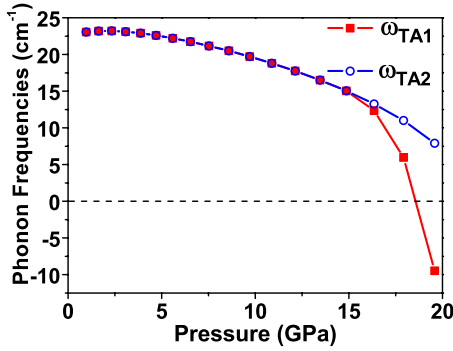


FIG. 1. (Color online) The pressure dependence of TA phonon frequencies at X point of the BZ boundary for PbTe crystal in $B1$ structure.

the highest valence band at the L point and gives rise to the topmost valence band in energy, the conduction-band minimum (CBM) and the next higher conduction band have the same L_6^- state, their mutual repulsion moves down the CBM, and thus the gap is shrunk. The band degeneracy at the high-symmetry k points is also lifted and band splitting could be observed in the anion and cation p states near Fermi level, as can be seen from the band structure of $B1$ phase in Fig. 4(a). In the $Pnma$ structure, the Te p -like bands are simply pushed upward below the Fermi level and the Pb p - and Te p -like bands are pushed downward above the Fermi level. In the $B1$ case, PW-PP LDA+SO scheme gives out energy band gap of 0.18 eV, very close to the experimental value 0.19 eV at 4 K.⁴⁶ In the FP-LAPW calculation, as is expected, EV-GGA+SO gives better band gap of 0.20 eV at the experimental lattice constants than PBE-GGA+SO result, 0.08 eV. While at theoretical equilibrium lattice constant, PBE-GGA+SO predicts band gap to be 0.22 eV, slightly larger than experimental value. The difference between the present FP-LAPW+SO band gaps and the values (0.16 eV) obtained by Albanesi *et al.*⁴⁷ are assumed to originate from a different XC potential that had been used in their work. In the $Pnma$ phase, the CBM is found along $\Gamma \rightarrow Z$ line, the valence-band maximum (VBM) locates at around T point, the indirect band gap in experimental lattice constants predicted by EV-GGA+SO is 0.22 eV, still closer to experimental band gap 0.355 eV at 77 K (Ref. 48) than the 0.11 eV predicted by PBE-GGA+SO. Note that the experimental

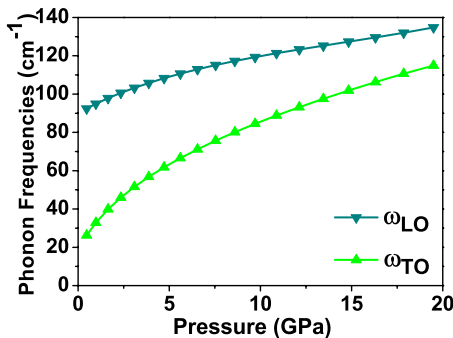


FIG. 2. (Color online) The pressure dependence of phonon frequencies at Γ point of the BZ for PbTe crystal in $B1$ structure.

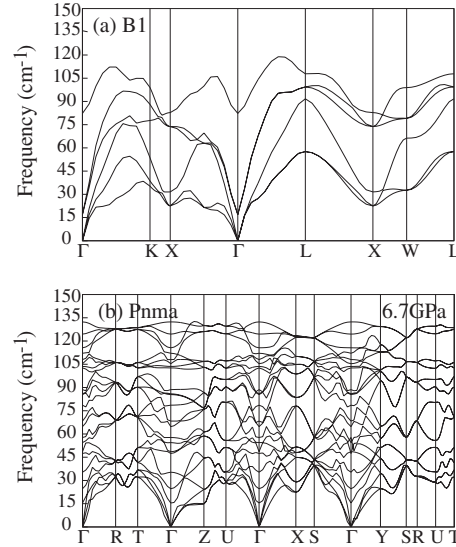


FIG. 3. Phonon dispersions for (a) PbTe within $B1$ phase at zero pressure; (b) PbTe within $Pnma$ phase at 6.7 GPa.

data 0.355 eV here is measured on thin-film layer, this should lead to some deviation from the bulk case, as calculated in this work. In the following energy-band calculations, lattice constants are set to experimental ones.

Another important thing should be noticed at Fig. 4(b) is that the band edge of $Pnma$ phase yields several electron pockets. The CBM is located at around $k = 2\pi(0, 0, 0.292c^*)$ along the $\Gamma \rightarrow Z$ line, one of electron pockets is found at Γ point with eigenenergy 0.17 eV higher than the CBM, another electron pocket is found at $k = 2\pi(0, 0, 0.5c^*)$ with eigenenergy 0.20 eV higher than the CBM. The other electron pockets can be observed with slightly higher energy. Note that at room temperature, the energy band approximately 0.2 eV around the chemical po-

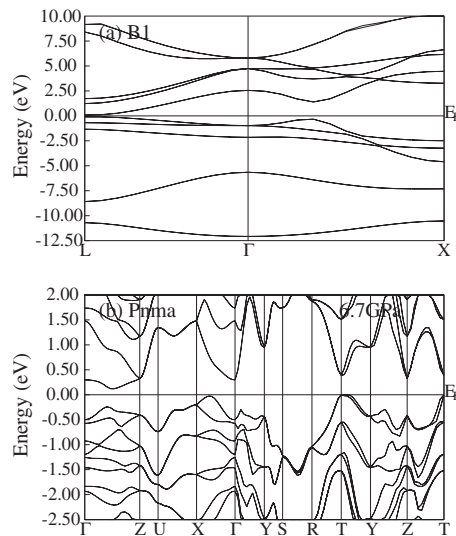


FIG. 4. Calculated electronic full relativistic band structure with spin-orbit interaction for PbTe. (a) Crystal in $B1$ structure, ambient condition. (b) Crystal in $Pnma$ structure, 6.7 GPa. The band spin-orbit splitting gives a better description of the band structure and band gap within the PBE-GGA approximation.

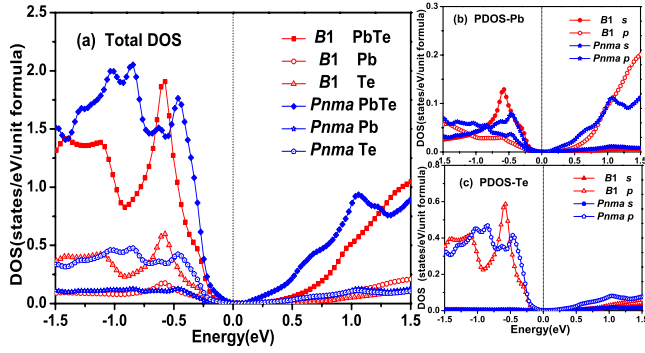


FIG. 5. (Color online) Calculated electron DOS for PbTe within the *B1* structure at ambient condition and *Pnma* structure at 6.7 GPa. (a) Total DOS for PbTe and projected DOS of Pb and Te atoms. (b) Projected DOS of *s* and *p* orbital components for Pb atom. (c) Projected DOS of *s* and *p* orbital components for Te atom.

tential will have significant contribution to the transport properties, these highly anisotropic electron pockets ensure large DOS and high group velocities simultaneously, which in turn lead to large Seebeck coefficient and electrical conductivities. This multivalley structure has been documented in literature and is believed to be preferable for TE materials.⁴⁹ Based on the multivalley band structure, PbTe in *Pnma* structure may be considered as a good candidate for TE applications.

Figure 5 presents the total and partial electronic density for the *B1* and *Pnma* phases. The VBM of both phases are set as zero for the sake of comparison. From the total DOS in Fig. 5(a), we can see that the valence states for both phases are separated from the conduction states by a small energy gap, with sharp increase in DOS along the gap edges. Similar behavior in projected DOS applies in the both structures, as depicted in Figs. 5(b) and 5(c). The conduction bands are mainly contributed from Pb 6*p* and Te 5*p* states while the valence bands are primarily from the Pb 6*s* and Pb 6*p* and Te 5*p* states. For the *p*- or *n*-doped compounds, Fermi level will shift down or up, respectively, therefore transport properties will be closely related to the electronic states near the VBM or CBM. It is clear in Fig. 5(a), the total DOS near the CBM for *Pnma* phase is much higher than that for the *B1* phase but the quantity is only comparable for both phases at around the VBM. Since larger DOS near the band gap is often associated with higher Seebeck coefficients, one can expect higher Seebeck coefficients in the *n*-type *Pnma* structure. Our calculations confirm this point, as discussed in more details in Sec. III D 1.

Energy band structure and band gap will have significant effect on the transport properties. EV-GGA is believed to give reasonable description of band gap; here we use this functional to perform a further calculation and analyze the effect of pressure on energy band gaps. Calculated band gaps from FP-LAPW EV-GGA+SO results with respect to pressure are presented in Fig. 6. The band gap of *Pnma* phase is larger than *B1* phase at equilibrium condition. With pressure applied both gaps narrows at first, leading to negative deformation potentials (band-gap pressure coefficient). Band gap of *B1* phase reaches its minimum at ~ 5.2 GPa, after that it

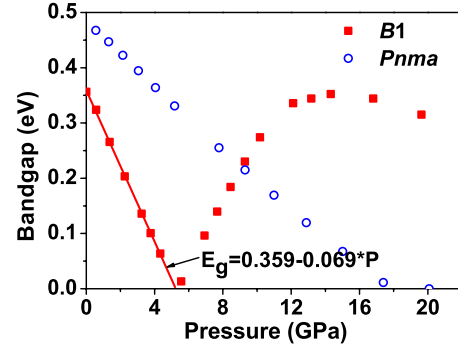


FIG. 6. (Color online) Band gap as a function of theoretical pressure for PbTe in *B1* phase (shown as solid squares) and *Pnma* phase (shown as open circles). Fitting the data points before gap closure one can get band-gap pressure coefficient, as shown in line and equation in the figure.

begins to increase again and finally surpass the *Pnma* phase. It is interesting to notice that there is previous report²¹ which claimed that at ~ 3 GPa bulk PbTe will become gapless, this is consistent with our calculation here. As the pressure increased band gap for *B1* phase closes first and reopens later while for *Pnma* phase only the closure is observed. We increased the pressure to above 40 GPa and no band-gap reopening for *Pnma* phase happens. What is more, we fitted deformation potentials $dE_g(L)/dP$ for *B1* phase before the close of band gap and got -6.85 meV/kbar, which is slightly larger than previous LDA calculation, -4.01 meV/kbar,⁵⁰ but very near to the experimental measurement -7.4 meV/kbar.⁵¹ Based on the above analysis, one can see that EV-GGA+SO gives pressure-induced band-gap modification of PbTe accurately.

D. Thermoelectric properties of PbTe

Before the transport calculation, a correction of band gap is needed. As is well known, the band gaps obtained by LDA or GGA calculations are usually underestimated when compared to the experimental ones. GW method can provide relative accurate quasiparticle energies but unfortunately, this approach requires very complex computations and is time consuming. The scissors operation^{52,53} offer an alternative mean by shifting the conduction bands up by a constant, which is believed to be a simple way to include the effect of the self-energy correction in the transport calculations. Considering the band-gap underestimation within the standard PBE-GGA functional, we choose EV-GGA to derive energy gaps and further correct band gaps according to experimental values. The shifting formula is

$$E_g = E_g(\text{EV-GGA}) - E_{g0}(\text{EV-GGA}) + E_{g0}(\text{Experiment}), \quad (3)$$

where E_{g0} denotes band gap at experimental lattice constants at ambient condition for *B1* phase and at 6.7 GPa for *Pnma* phase.

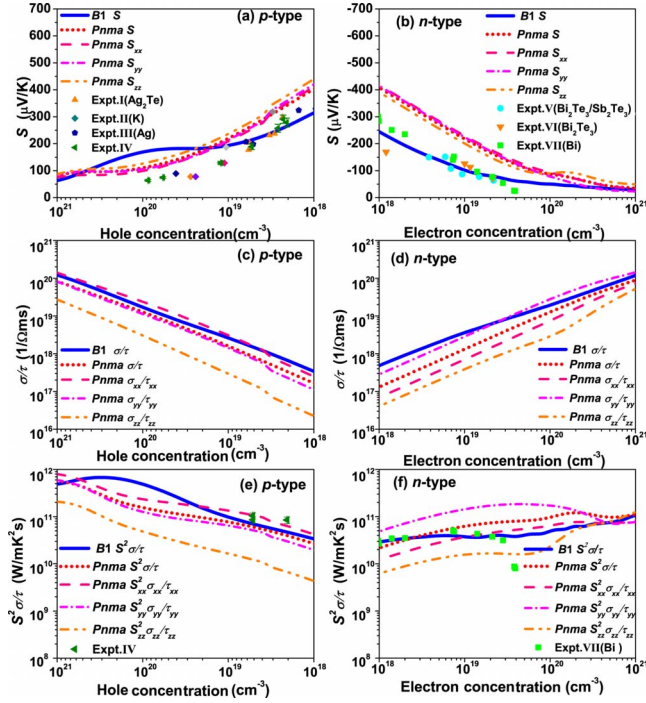


FIG. 7. (Color online) Calculated thermoelectric properties of PbTe at 300 K within the *B1* structure at ambient pressure and *Pnma* structure at 6.7 GPa, as a function of carrier concentrations. (a) *p*-type Seebeck coefficients, S . (b) *n*-type Seebeck coefficients, S . (c) *p*-type electrical conductivity with respect to relaxation time, σ/τ . (d) *n*-type electrical conductivity with respect to relaxation time, σ/τ . (e) *p*-type power factor with respect to relaxation time, $S^2\sigma/\tau$. (f) *n*-type power factor with respect to relaxation time, $S^2\sigma/\tau$. The transport coefficients for *B1* and *Pnma* phases are shown as solid lines; the xx , yy , and zz components of the transport tensors for *Pnma* phase are shown as dashed, dashed-dotted, and dashed-dotted-dotted lines; the experimental data Expt.I (Ref. 54), Expt.II (Ref. 55), Expt.III (Ref. 56), Expt.IV (Ref. 57), Expt.V (Ref. 58), Expt.VI (Ref. 59), and Expt.VII (Ref. 7) are shown as symbols. The dopants in PbTe are shown in brackets.

1. Thermoelectric properties at ambient condition

The calculated transport coefficients at various doping level at 300 K for *B1* phase under ambient pressure and *Pnma* phase at 6.7 GPa are illustrated as lines in Fig. 7. Computational results can be verified by comparing with the experimental ones.^{7,54–59} Very few experimental reports on *Pnma* structure were found, so we only present some available experimental data on *B1* phase as scatters in Fig. 7 for comparison. The theoretical Seebeck coefficients of *p*-type PbTe in the low hole concentration region well reproduce the experimental trend whereas in the high concentration domain, large discrepancy between theory and experiment is observed [Fig. 7(a)]. In view of the discrepancy in the high hole concentration part, overestimation of power factor and ZT will be expected. For *n*-type PbTe, the calculated S agrees well with experimental values in the overall doping range [Fig. 7(b)]. The electrical conductivity of bulk lead telluride is sensitive to doping, as can be seen from Figs. 7(c) and 7(d) that σ/τ adopts a logarithm increase with carrier concentration. Therefore doping level selection will be an important

option for optimizing TE properties. *B1* phase has larger σ/τ than *Pnma* phase, which makes up for its Seebeck coefficients S in *p*-doping case, and thus lead to quite large power factor [Fig. 7(e)]. The transport tensors for *Pnma* phase are highly anisotropic. The best TE performance is found at xx and yy directions for *p*-type and *n*-type compounds, respectively. From the comparison of the figures, we can find that S and $S^2\sigma/\tau$ of *n*-type *Pnma* phase are much higher than that of *n*-type *B1* phase [Figs. 7(b) and 7(f)], which should attribute to the higher DOS in the *Pnma* structure near the CBM. An opposite influence of doping on σ/τ can also be observed. With the increase in doping amount S decreases whereas σ/τ increases smoothly. The significant contradictory effects of doping on S and σ/τ will lead to a subtle variation in power factor especially in the high doping level, although a trend of power factor enhancement can be clearly observed with increasing doping. For the sake of comparison, the experimental power factors^{7,57} are divided by relaxation time and compared with theoretical one. They are in reasonable agreement with each other except the data at $4 \times 10^{19} \text{ cm}^{-3}$ for *n*-type PbTe. For that anomaly data point, it may come from experimental uncertainty, or from uniform parameters we used in deriving the relaxation time in the Kane model. Actually relaxation time changes slightly as the carrier concentration varies.

Why do both structures possess good transport properties but one is isotropic while the other is anisotropic? It should be linked with their crystal structures and related electronic properties. The energy band and DOS have shown the characters of narrow band gap, multivalley, sharp band-edge natures, which are favored for good TE property. The total DOS of Pb and Te atoms [Fig. 5(a)] are strongly overlapped in both phases, indicating remarkable covalent bonding character between Pb and Te. This can be illustrated more clearly in the deformation electron charge densities, as shown in Fig. 8. The strong charge accumulation along the Pb-Te bonding direction [Figs. 8(a) and 8(b)] implies covalent bonding behavior. The crystal structure of *B1* phase [Fig. 8(c)] depicts the sixfold coordination while the crystal structure of *Pnma* phase [Fig. 8(d)] shows that the atoms are displaced from the ideal *B1* structure, the Pb(Te) atoms are surrounded by 7 Te(Pb) atoms, as well as two Pb(Te) atoms at slightly larger distances. At 6.7 GPa, these seven neighbors are located at distances ranging from 2.93 to 3.81 Å.²⁰ It is also found that the charge accumulation takes place along the atomic distorting direction [Fig. 8(b)], which indicates the stronger covalent bonding in *Pnma* structure. It was previously reported that in semiconductors the highest mobility of the charge carriers is associated with the covalent bonding.⁶⁰ Also it is noteworthy that covalent bonds are thought to be favorable for thermoelectricity.¹³ These bonding characters, together with energy-band structure would contribute to a good TE performance. What is more, the anisotropic crystal and electronic nature of *Pnma* phase is responsible for its direction-dependent transport properties.

In principle, the relaxation time should be different for electrons and holes. Changes in microstructure or space-group symmetry could also induce deviations. Unfortunately, there is lack of information about this issue. In order to proceed further calculations for ZT , here we assume that the

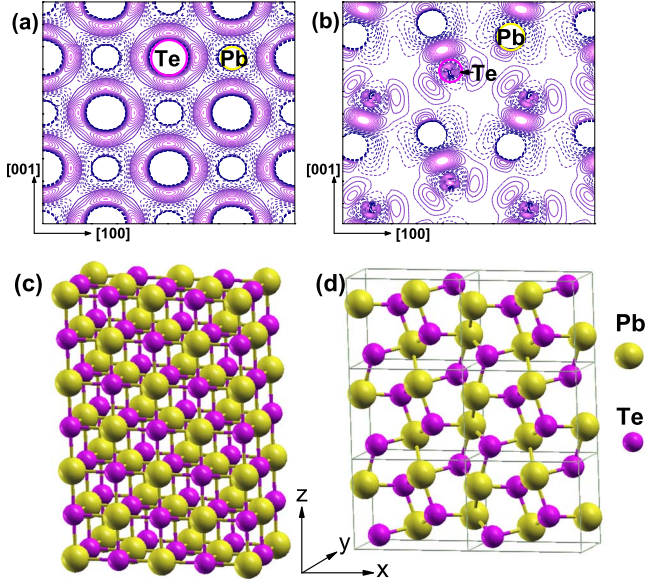


FIG. 8. (Color online) Deformation charge densities in the (010) plane for PbTe within (a) *B1* phase and (b) *Pnma* phase. Contour range: -0.05 – 0.05 $e/\text{\AA}^3$, contour interval: 0.005 $e/\text{\AA}^3$, solid/dotted contours: positive/negative. Crystal structure of PbTe within (c) *B1* phase and (d) *Pnma* phase.

value of relaxation time is independent of structures or phases. Figure 9 presents ZT (as obtained using aforementioned methods) versus carrier concentrations of *p*- and *n*-type PbTe at 300 and 600 K, where Lorentz number is set as $L_0 = (156 \mu\text{V}/\text{K})^2$, lattice thermal conductivity is chosen from available experimental report on bulk PbTe, i.e., $\kappa_l = 2.0$ W/mK and 1.42 W/mK for 300 K and 600 K, respectively.⁶¹ The experimental values on *n*-type PbTe within *B1* phase⁶² is plotted as symbols for comparison. Note that the experimental and theoretical values do not coincide with each other well, and ZT at 600 K cases are rather high, due to some reasons as discussed below. We note that Lorentz number increase with increasing doping level and decrease with increasing temperature while in our calculation it is fixed as a constant. The choice of Lorentz number could yield some error. Lattice thermal conductivity is also set as a constant value in the calculation. As a matter of fact, it varies with respect to carrier concentration. Relaxation time derived from Kane model could also introduce some deviations, ZT is sensitive to the parameters used in the model. Nevertheless, the overall trends of ZT on doping level for experiment and theory are the same. If we only use the results to predict when, where, and how can the optimized ZT appear, this discrepancy is acceptable and the conclusion is reliable. To achieve high power factor and ZT values an appropriate carrier concentration is demanded, ideally it is preferred to be above 10^{19} cm^{-3} . From Fig. 9 we find that as doping increases, ZT is improved first and attenuated later. The first increase in ZT could be attributing to the increase in electrical conductivity σ . When it comes to the higher doping level, S goes toward its minimum and the electronic scattering becomes dominant, resulting in dramatic decrease in the figure of merit. Therefore the optimized performance appears at middoping region. At 600 K, for *B1* phase, the best ZT per-

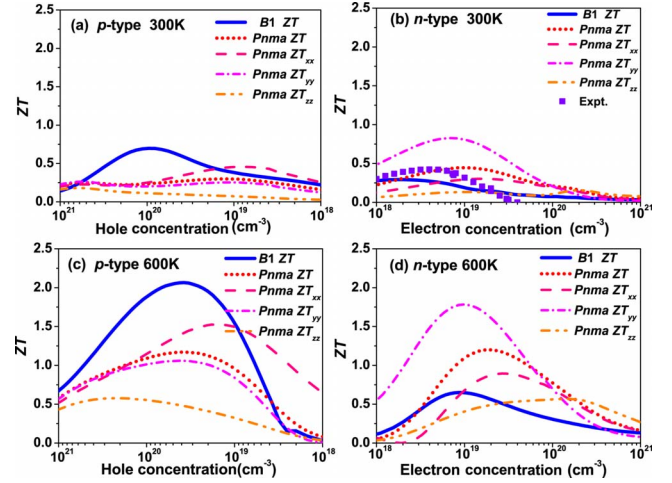


FIG. 9. (Color online) The calculated ZT versus carrier concentrations at 300 and 600 K for PbTe within the *B1* structure at ambient pressure and *Pnma* structure at 6.7 GPa. The transport coefficients for *B1* and *Pnma* phases are shown as solid lines; the xx , yy , and zz components of the transport tensors for *Pnma* phase are shown as dashed, dashed-dotted and dashed-dotted-dotted lines; the experimental data from Ref. 62 are shown as symbols for comparison. The lattice thermal conductivity κ_l is chosen to be 2.0 W/mK and 1.42 W/mK for 300 K and 600 K, respectively. The relaxation time τ is obtained by Eq. (1).

formance appears at nominal $n_h \approx 4.0 \times 10^{19}$ cm^{-3} and $n_e \approx 0.9 \times 10^{19}$ cm^{-3} ; for *Pnma* phase the highest ZT value is found with nominal $n_h \approx 1.35 \times 10^{19}$ cm^{-3} along xx direction and $n_e \approx 1.0 \times 10^{19}$ cm^{-3} along yy direction. Considering the deviation caused by relaxation time and thermal conductivity, these theoretical values are in reasonable agreement with experimental measurements.

Traditionally PbTe in *B1* structure is expected to be *n*-type TE material since the mobility of electrons in the Pb-based conduction band is greater than that of holes in the Te-based valence band. Our calculation results show that *n*-type PbTe within *Pnma* phase has even better TE performance than *B1* phase. The maximum ZT for *Pnma* structure at 300 K is about 0.83 along the yy direction, nearly 2.7 time of maximum ZT for *B1* structure (~ 0.30). For the *B1* phase, ZT values of *p*-type materials are much higher than that of *n*-type compounds. ZT reaches its maximum of 0.7 at a concentration of $n_h \approx 9.6 \times 10^{19}$ cm^{-3} at 300 K, which is more than two times of that of *n*-type value. With these observations, one might expect *p*-type PbTe within the NaCl structure will have superior performance in TE applications.

From Eq. (2) we also calculated the ZT values versus temperature at fixed carrier concentrations for PbTe within *B1* phase at ambient pressure and *Pnma* phase at 6.7 GPa. The calculated Seebeck coefficient, power factor and ZT values as a function of temperature for several carrier concentrations are shown at Fig. 10. Since few experimental reports on the TE properties of *Pnma* phase is found, here we only present the calculated ZT values and compare it with *B1* phase, other TE properties for *Pnma* phase are omitted. In this part, the lattice thermal conductivity is chosen to be $\kappa_l = 2.0$ W/mK for the overall temperature range. Note that

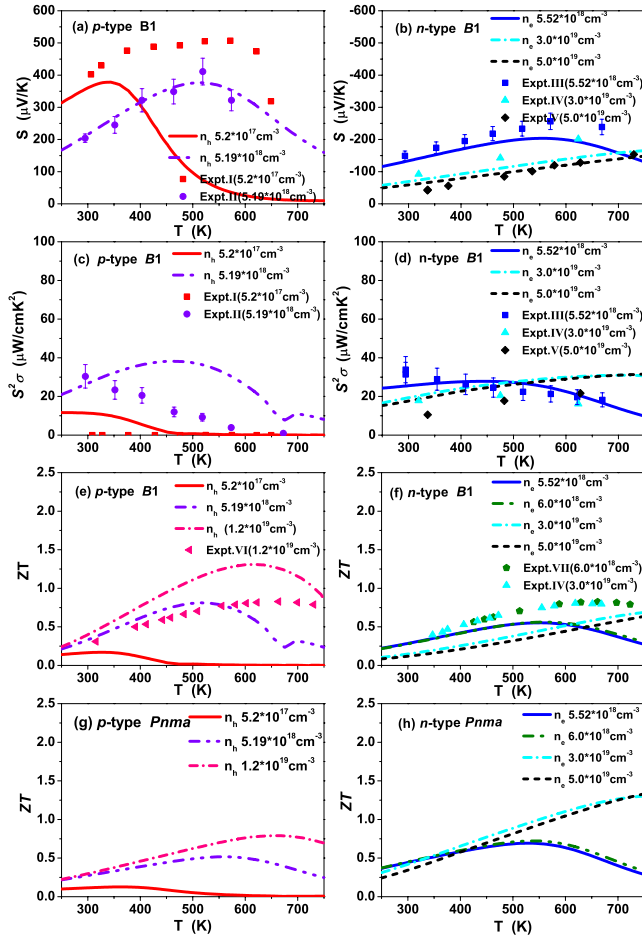


FIG. 10. (Color online) Temperature dependence of (a) Seebeck coefficients, S ; (c) power factor, $S^2\sigma$; (e) ZT for p -type PbTe within $B1$ phase and (g) ZT for p -type PbTe within $Pnma$ phase at concentrations $n_h = 5.0 \times 10^{17} \text{ cm}^{-3}$, $5.19 \times 10^{18} \text{ cm}^{-3}$, $1.2 \times 10^{19} \text{ cm}^{-3}$. Temperature dependence of (b) Seebeck coefficients, S ; (d) power factor, $S^2\sigma$; (f) ZT for n -type PbTe within $B1$ phase and (h) ZT for n -type PbTe within $Pnma$ phase at concentrations $n_e = 5.52 \times 10^{18} \text{ cm}^{-3}$, $6.0 \times 10^{18} \text{ cm}^{-3}$, $3.0 \times 10^{19} \text{ cm}^{-3}$, $5.0 \times 10^{19} \text{ cm}^{-3}$. Theoretical values are shown as solid lines and experimental values are shown as solid symbols. The lattice thermal conductivity κ_l used to calculate ZT is set to 2.0 W/mK. Experimental data for Expt. I ($n_h = 5.0 \times 10^{17} \text{ cm}^{-3}$), Expt. II ($n_h = 5.19 \times 10^{18} \text{ cm}^{-3}$), Expt. III ($n_e = 5.52 \times 10^{18} \text{ cm}^{-3}$), Expt. IV ($n_e = 3.0 \times 10^{19} \text{ cm}^{-3}$), Expt. V ($n_e = 5.0 \times 10^{19} \text{ cm}^{-3}$), Expt. VI ($n_h = 1.2 \times 10^{19} \text{ cm}^{-3}$), Expt. VII ($n_e = 6.0 \times 10^{18} \text{ cm}^{-3}$) are collected from Refs. 63, 57, 65, 66, and 64, respectively.

both L and κ_l decreases as temperature increases, corrections should be made at the high-temperature region when compared with experimental values. The calculated p -doping Seebeck coefficients [Fig. 10(a)] are in good agreement with experimental measurements.^{57,63} The theoretical power factor of p -type PbTe [Fig. 10(c)] with nominal $n_h = 5.2 \times 10^{17} \text{ cm}^{-3}$ does not seem to agree well with experimental report from Zhou *et al.*⁶³ Reasons may be due to the fact that the sample measured at their work is a thin-film layer, TE properties in bulk and film appearance should have some difference. Also the relaxation time τ can introduce some errors. The smaller experimental report from Bayer's⁶⁴ of ZT

[Fig. 10(e)] with $n_h = 1.2 \times 10^{19} \text{ cm}^{-3}$ is calculated with $\kappa_l = 2.5 \text{ W/mK}$, which is higher than the lattice thermal conductivity we used, hence our ZT should be a little bit larger than their result. In the n -doping case the calculated Seebeck coefficient [Fig. 10(b)] is somewhat slightly smaller than the experimental result.^{57,65,66} The theoretical power factor are well consistent with experimental ones [Fig. 10(d)] but with smaller S underestimated ZT could be expected [Fig. 10(f)]. The high-temperature ZT values [Fig. 10(f)] of n doping at $n_e = 6.0 \times 10^{18} \text{ cm}^{-3}$ are much smaller than the experimental report because in Ref. 64, a smaller Lorentz number is used for temperatures above 570 K, while in our situation it is the same as low temperatures. Considering the errors come from relaxation time and thermal conductivity, the overall agreement between theoretical and experimental values at different nominal carrier concentrations is satisfactory.

From the comparison of Figs. 10(e)–10(h) we can see that in the whole temperature range, n -type $Pnma$ PbTe has larger ZT values than the $B1$ case while in p -doping situation it is smaller. This could be owing to the larger DOS for $Pnma$ phase at around CBM and comparable DOS at around VBM but larger σ/τ for $B1$ phase. The optimal carrier concentration should be $n_h > 1.2 \times 10^{19} \text{ cm}^{-3}$ and $n_e < 3.0 \times 10^{19} \text{ cm}^{-3}$ for both phases. All these results are consistent with conclusions drawn from Fig. 9.

To get a vivid picture, three-dimensional (3D) contour distributions of S , σ/τ , $S^2\sigma$ and ZT as a function of temperature and carrier concentration for $B1$ phase at ambient pressure and $Pnma$ phase at 6.7 GPa are illustrated in Fig. 11. The hotter the pattern is, the higher the physical quantity is. The contour maps in the last line represent ZT , it is worthy to stress that there is no single optimal doping level for entire working temperature range, or one single optimal working temperature for entire doping range. From the comparison of the patterns, we can also see that in the p -doping case, although $Pnma$ phase possesses higher S than $B1$ phase, its p -type electrical conductivity is much smaller than that of $B1$ phase, thus its power factor and ZT are smaller. In the n -doping situation, however, $Pnma$ phase possesses higher S than and comparative σ to $B1$ phase, therefore its power factor and ZT are higher. At low doping level, optimal ZT occurs at 300–450 K temperature range. With the doping level increased, the optimal ZT point shifts to higher temperature domain. The optimal doping level is $1.0 \times 10^{19} \text{ cm}^{-3}$ – $1.0 \times 10^{20} \text{ cm}^{-3}$, and the optimal working temperature is above 650 K for $B1$ phase and above 700 K for $Pnma$ phase. Recently Singh⁶⁷ made a calculation on doping dependence and temperature dependence of the thermopower, our results on this issue are consistent with their reports.

2. Effect of band gap on thermoelectric properties

Because of strong electron-phonon coupling, lead telluride is known to have temperature-dependent energy band gap. Experimentally one finds E_g increases linearly with temperature for $T \leq 400 \text{ K}$ in $B1$ structure,³⁹

$$E_g = \begin{cases} 0.19 + (0.42 \times 10^{-3})T & T \leq 400 \text{ K}, \\ 0.358 & T > 400 \text{ K}. \end{cases} \quad (4)$$

and for $T \leq 320 \text{ K}$ in $Pnma$ structure,⁴⁸

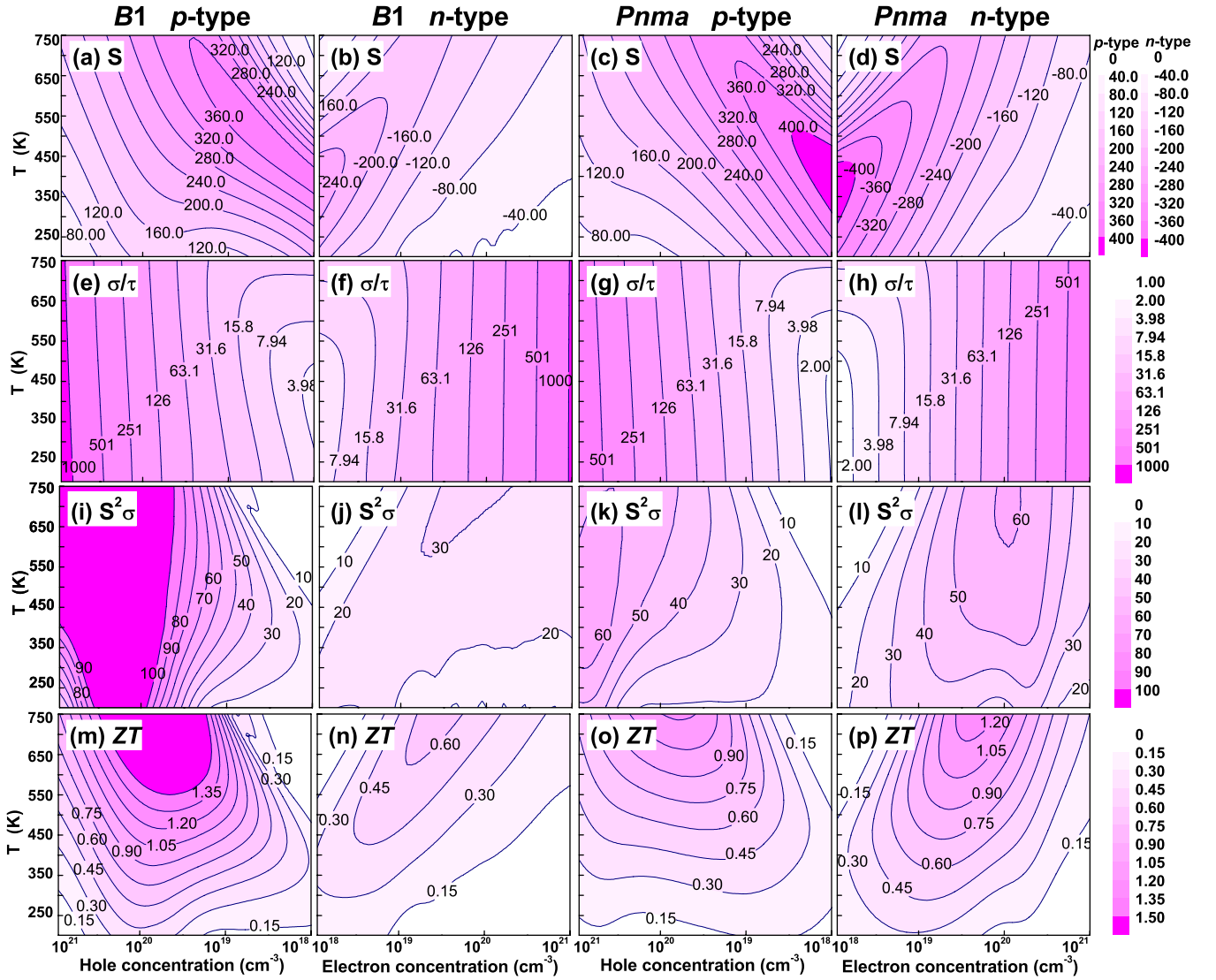


FIG. 11. (Color online) Contour distributions of transport properties on temperature and carrier concentration. (a)–(d) Seebeck coefficients, S ($\mu\text{V}/\text{K}$). (e)–(h) electrical conductivity with respect to relaxation time, σ/τ [10^{17} ($\Omega \text{ ms})^{-1}$]. (i)–(l) power factor, $S^2\sigma$ ($\mu\text{W}/\text{cm K}^2$). (m)–(p) ZT values, dimensionless. Subplots (a), (e), (i), and (m) are results for p -type B1 phase; (b), (f), (j), and (n) are results for n -type B1 phase; (c), (g), (k), and (o) are results for p -type $Pnma$ phase; (d), (h), (l), and (p) are results for n -type $Pnma$ phase; respectively. The lattice thermal conductivity used to calculate ZT is set to $\kappa_l=2.0$ W/mK. The maximum for each situation is perched at the hottest area within each subplot, where the optimal combination of carrier concentration and working temperature locates.

$$E_g = 0.332 + (0.2762 \times 10^{-3})T \quad T < 320 \text{ K.} \quad (5)$$

To clarify the effect of band gap on transport properties, we investigated the thermoelectric performance of PbTe with different band gaps at 300 and 600 K, results are presented in Fig. 12. B1 phase is calculated at ambient condition and $Pnma$ phase at 6.7 GPa. A constant relaxation time $\tau=4.48 \times 10^{-14}$ s (Ref. 18) is used here. This parameter should be a little larger at the high-temperature situation and overestimated ZT will be expected for 600 K case. But we are short of experimental reports which can be used to derive temperature or doping dependent τ , therefore these ZT values can only provide a baseline for understanding the band-gap dependence of TE properties. Lattice thermal conductivity is set as $\kappa_l=2.0$ W/mK at 300 K and 1.42 W/mK at 600 K. In the 300 K situation, with larger band gap, S of lower carrier

concentrations ($1.0 \times 10^{15} - 5.0 \times 10^{17} \text{ cm}^{-3}$) is greatly improved while $S^2\sigma$ and ZT are only slightly enhanced. Reasons should be in the focus of low electrical conductivity here. For higher carrier concentration, difference between large and small band gaps is negligible. This result is similar to Ref. 18. High-temperature instance is not analyzed in Ref. 18. Our calculations reveal that it behaves a little different. In 600 K case, as the band gap enlarged, S is enhanced at mid-to-high doping range (carrier concentration between 1.0×10^{17} and $1.0 \times 10^{20} \text{ cm}^{-3}$). Although the magnitude is smaller than the 300 K instance, the electrical conductivity here is much larger than in the low carrier concentration situation, therefore significant improvement are achieved in power factor and ZT . Note that, in Fig. 12, left and right y axis corresponds to 300 and 600 K cases, respectively, and the scale of right y axis (related to 600 K case) is five times

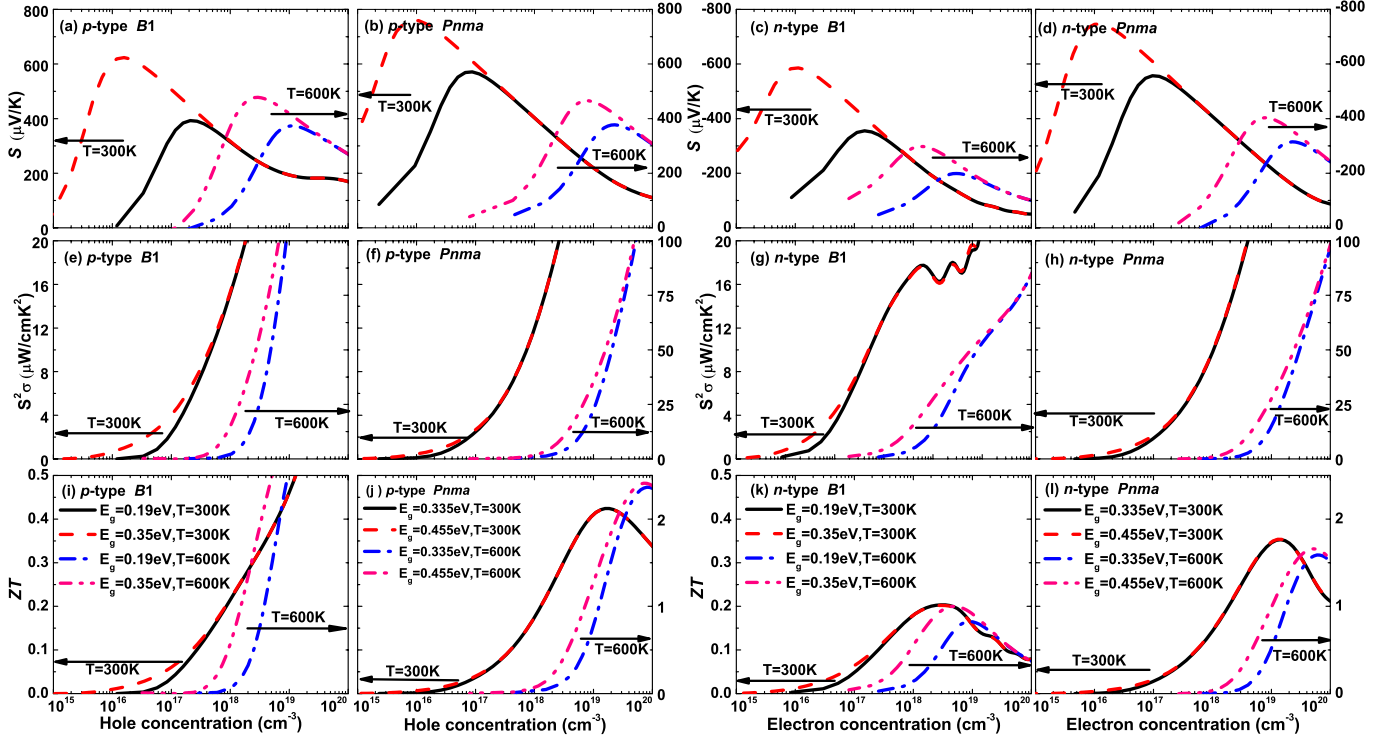


FIG. 12. (Color online) Effect of band gap on transport properties at 300 and 600 K in B1 and *Pnma* structures. (a)–(d) Seebeck coefficients, S . (e)–(h) power factor, $S^2\sigma$. (i)–(l) ZT values. The band gaps in B1 structure are set to 0.19 eV and 0.358 eV, corresponding to minimum and maximum experimental records. The band gaps in *Pnma* structure are set to 0.335 and 0.435 eV, according to experimental reports. The relaxation time τ used here is 4.48×10^{-14} s, this may result in overestimated ZT at high temperature but cannot alter the conclusions. Lattice thermal conductivity is set as $\kappa_l = 2.0$ W/mK and 1.42 W/mK for 300 K and 600 K, respectively. Subplots (a), (e), and (i) are results for *p*-type B1 phase; (b), (f), and (j) are results for *p*-type *Pnma* phase; (c), (g), and (k) are results for *n*-type B1 phase; (d), (h), and (l) are results for *n*-type *Pnma* phase; respectively. The scale of right y axis (corresponds to 600 K case) is five times of the left y axis (related to case of 300 K) for $S^2\sigma$ and ZT . Legends for S , $S^2\sigma$ are the same as ZT and are presented only once within each column. The 300 K results indicate band-gap width is negligible for carrier concentration higher than 1.0×10^{18} cm^{-3} while the 600 K results suggest band-gap width can have strong influence on TE performance for carrier concentration up to 1.0×10^{20} cm^{-3} .

of the left (related to case of 300 K) for $S^2\sigma$ and ZT . In *n*-type B1 case, effect of band gap on TE properties can only be omitted for $n_e \geq 3.0 \times 10^{19}$ cm^{-3} ; for others it is about $n_e \geq 1.0 \times 10^{20}$ cm^{-3} . Band-gap correcting is highly recommended in transport calculation when temperature is large.

TE properties for PbTe under pressure within different band gaps are also studied; similar 3D distributions like Fig. 11 can be obtained (not shown). Between low-to-mid pressure ranges, observable enhancement can be seen; under high pressure it disappears. From the calculation of both *p*- and *n*-type systems, we found that the choice of band gaps affects significantly the transport calculation, at room temperature the effect is negligible for concentrations higher than 1.0×10^{18} cm^{-3} ; at high temperature the effect extends to higher doping level.

3. Effect of pressure on thermoelectric properties

Pressure induced structural transition normally involves changes in space-group symmetry or phases; deformations of the crystal microstructures. The microelectronic structure modifications can lead to the alteration in band structure, band gap, and Fermi surface, etc. It is well known that even the slight changes in band structure and Fermi surface can

have an effect on the transport properties. For example, the Seebeck coefficient is related to the derivatives of the electronic density of states near the Fermi level. Pressure induced band-gap change has been discussed in Sec. III C. With the pressure induced band-gap closure and reopening, thermoelectric properties are expected to follow different rules under different pressure. Since we are lack of knowledge about κ_l and τ under pressure, we had to assume the ambient pressure one.

Figure 13 presents the contour distributions of S , $S^2\sigma/\tau$, $S^2\sigma$ and ZT as a function of pressure and carrier concentration for B1 phase at 300 and 600 K. Seebeck coefficient has an unusual behavior at around 5–8 GPa. As is known that thermoelectric power or Seebeck coefficient is sensitive to the microstructural state, a sharp increase or decrease in its performance may indicate phase transition. The pressure range where the abnormality appears matches the critical pressure needed for [B1(NaCl) \rightarrow *Pnma*] transition. Another interesting thing is that the best TE performance for *p* doping sits at ~ 8 GPa; while for *n* doping it is above 18 GPa. At ambient condition, *n* doping has lower S , $S^2\sigma$ and ZT values than *p* doping; under high pressure, both S and $S^2\sigma$ are improved, resulting in inspiring ZT performance.

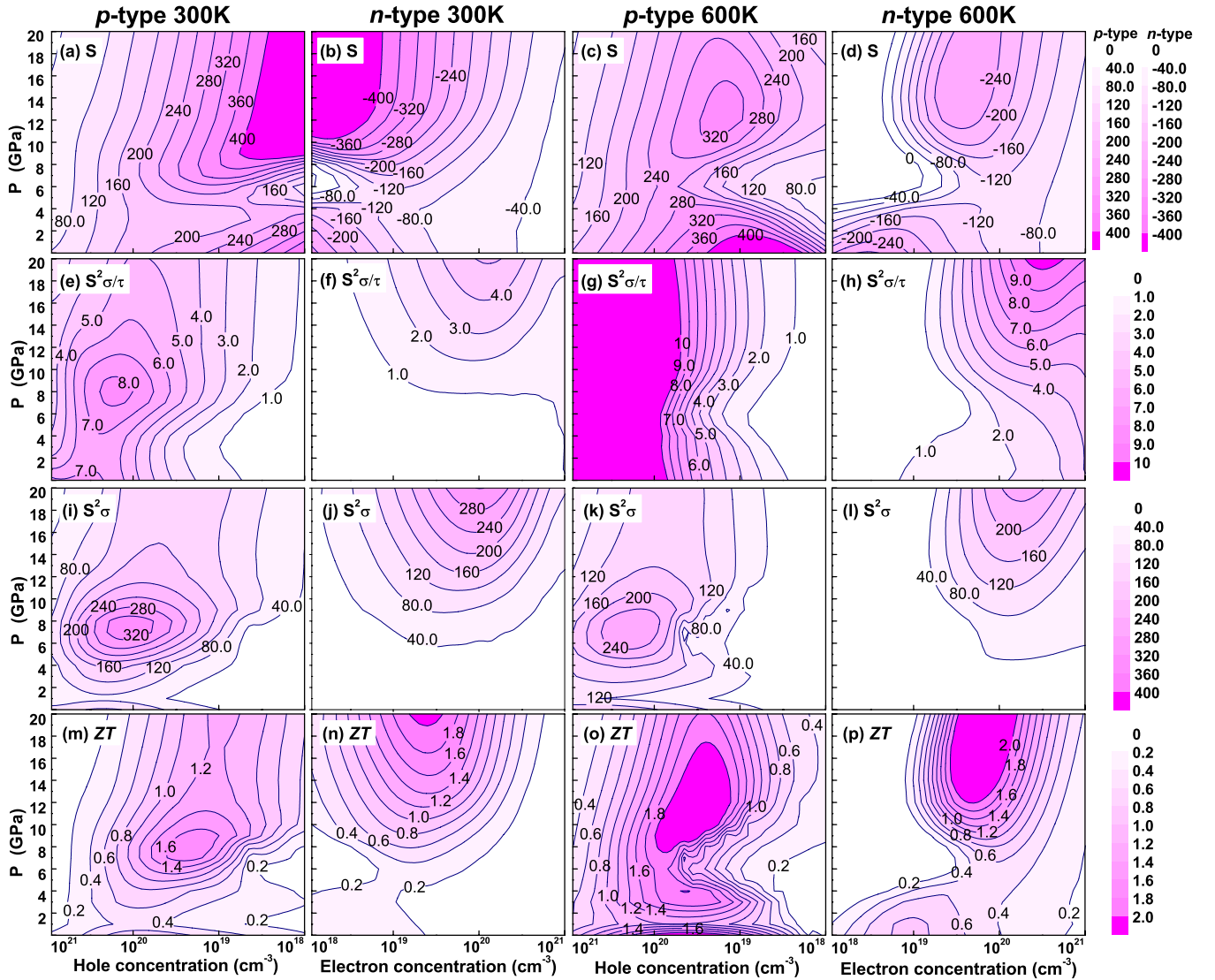


FIG. 13. (Color online) Contour distributions of transport properties on theoretical pressure and carrier concentrations at 300 and 600 K in $B1$ structure. (a)–(d) Seebeck coefficients, S ($\mu\text{V}/\text{K}$). (e)–(h) power factor with respect to relaxation time, $S^2\sigma/\tau$ ($10^{15} \mu\text{W}/\text{cm}^2 \text{K}^2 \text{s}$). (i)–(l) power factor, $S^2\sigma$ ($\mu\text{W}/\text{cm}^2 \text{K}^2$). (m)–(p) ZT values, dimensionless. Subplots (a), (e), and (m) are results for 300 K p -type case; (b), (f), (j), and (n) are results for 300 K n -type case; (c), (g), (k), and (o) are results for 600 K p -type case; (d), (h), (l), and (p) are results for 600 K n -type case; respectively. The lattice thermal conductivity used to calculate ZT is set to $\kappa_l=2.0$ W/mK and 1.42 W/mK at 300 K and 600 K, respectively. The maximum for each situation is located at the focus of the hottest area within each subplot, where the optimal combination of carrier concentration and working pressure is.

The three-dimensional TE properties for $Pnma$ phase at 300 and 600 K under pressure are also presented at Fig. 14. S has a decreasing trend with pressure. ZT is not as sensitive to pressure as in the $B1$ instance. In the high doping region, it remains nearly unchanged with increasing pressure. The optimal ZT performance at 600 K is found at 6–8 GPa and 4.0×10^{19} – $6.0 \times 10^{19} \text{ cm}^{-3}$ doping level. General speaking p -type PbTe in $Pnma$ structure is not competitive with $B1$ case but the n -type PbTe in $Pnma$ structure under low-pressure range has better performance than $B1$ case. The optimal doping level at 600 K is higher than that at 300 K for both phases.

Seebeck coefficients as a function of pressure for several carrier concentrations at 300 and 600 K are also presented [Figs. 15(a)–15(h)]. Evidence of phase transition may be ob-

served when the thermoelectric power has a steep increase or decrease near the transition point. The room-temperature low-doping Seebeck coefficients do possess a sharp increase after passing through the critical pressure at ~ 6 GPa [Fig. 15(a)]. This decrease-increase behavior can be observed in both p -type and n -type material within $B1$ phase while only a monotonically decreasing trend is found for materials within $Pnma$ structure. The values of experimental report by Ovsyannikov *et al.*¹⁹ is also showed as open symbols [Fig. 15(c)], which shows Seebeck coefficients of n -type bulk PbTe decrease as the pressure increase. Only the first half part seems to agree with the results obtained here. Since we are short of data about sample's doping level, no further comparisons can be made.

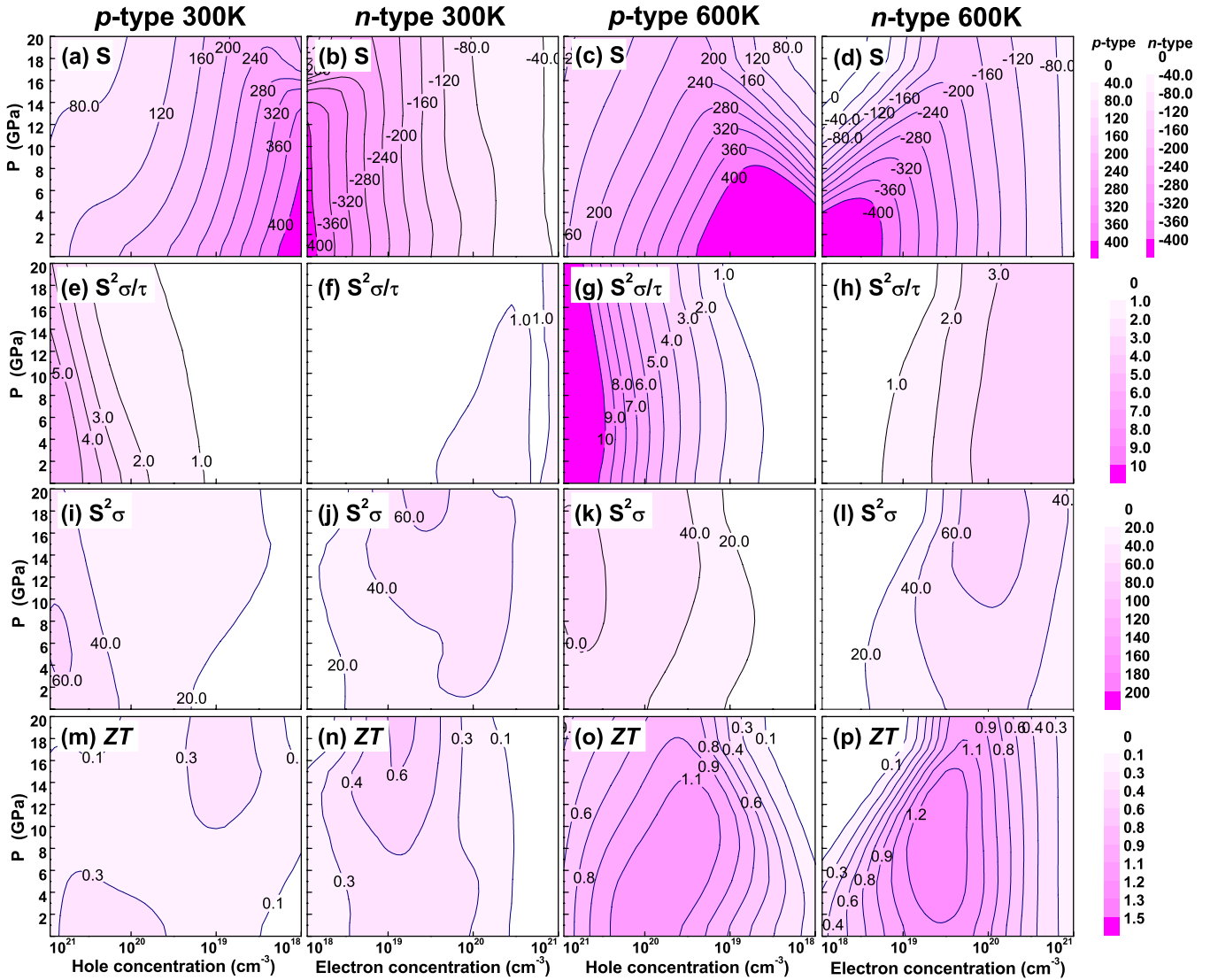


FIG. 14. (Color online) Contour distributions of transport properties on theoretical pressure and carrier concentration at 300 and 600 K within $Pnma$ structure. (a)–(d) Seebeck coefficients, S ($\mu\text{V}/\text{K}$). (e)–(h) power factor with respect to relaxation time, $S^2\sigma/\tau$ ($10^{15} \mu\text{W}/\text{cm}^2 \text{K}^2 \text{s}$). (i)–(l) power factor, $S^2\sigma$ ($\mu\text{W}/\text{cm}^2 \text{K}^2$). (m)–(p) ZT values, dimensionless. The same as Fig. 13 except that results are for $Pnma$ phase.

In Figs. 15(i)–15(p), we present ZT values as a function of pressure for several carrier concentrations at 300 and 600 K. In the $B1$ circumstance, with the reopening of band gap p -type ZT goes to its maximum and decreases under high pressure while n -type ZT adopts a simple increasing trend with pressure. The calculated ZT values are predicted to show an anomaly at ~ 6 GPa, which is close to the band-gap inversion pressure. At low-pressure domain ZT of 600 K is higher than that of 300 K while at the high-pressure region it is smaller. In the $Pnma$ case, except for the low-doping cases ZT remains nearly unchanged with respect to pressure. One possible explanation is that this phase possesses no gap reopening at the pressure range where our calculations are performed. From all the above analysis, we can come to a conclusion that pressure can offer another effective way for optimizing TE performance.

IV. CONCLUSIONS

In this paper, we have performed first-principles *ab initio* calculations to study the electronic and lattice dynamics properties of lead telluride in $B1$ and $Pnma$ structures. Dynamical analysis on the $B1$ phase at the ambient condition revealed that there exists anharmonic instability of the optical branch at the zone center. The \mathbf{k} -dependent soft modes may be responsible for the thermal conductivity change under pressure. The soft phonons at the BZ boundary X point are linked with particular $[B1 \rightarrow B2]$ phase transition. In the transport calculations we found that p -type PbTe within $B1$ phase at ambient condition has the best TE quality while n -type PbTe within $Pnma$ phase at 6.7 GPa has better performance than the $B1$ structure. The physical origin is mainly from the special band structure for $B1$ and $Pnma$ phases, namely, larger DOS near the CBM for $Pnma$ phase, and

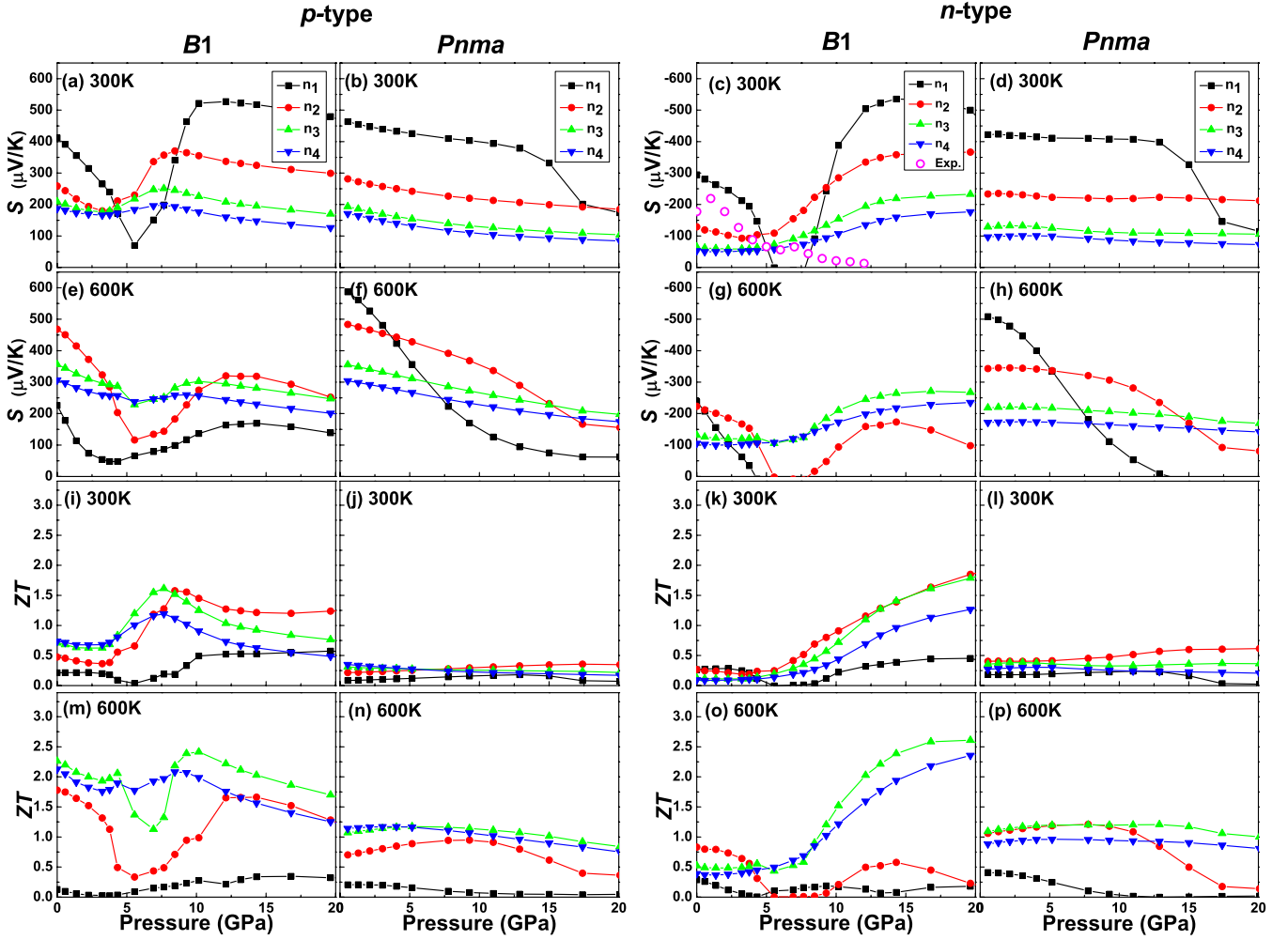


FIG. 15. (Color online) Seebeck coefficients S as a function of pressure for different carrier concentrations at: (a)–(d) 300 K and (e)–(h) 600 K in B1 and $Pnma$ structures. And ZT values as a function of pressure for different carrier concentrations at: (i)–(l) 300 K and (m)–(p) 600 K in B1 and $Pnma$ structures. Subplots (a), (e), (i), and (m) are results for p -type B1 phase; (b), (f), (j), and (n) are results for p -type $Pnma$ phase; (c), (g), (k), and (o) are results for n -type B1 phase; (d), (h), (l), and (p) are results for n -type $Pnma$ phase; respectively. The lattice thermal conductivity used to calculate ZT is set to $\kappa_l = 2.0$ W/mK and 1.42 W/mK at 300 K and at 600 K case. Legends for the four subfigures in the same column are the same and therefore only presented once in the first line. Carrier concentrations: $n_1 = 1.0 \times 10^{18}$ cm $^{-3}$, $n_2 = 1.0 \times 10^{19}$ cm $^{-3}$, $n_3 = 5.0 \times 10^{19}$ cm $^{-3}$, $n_4 = 1.0 \times 10^{20}$ cm $^{-3}$. Experimental data collected from Ref. 19 are shown as open circles, where the electron concentration for the sample is unknown. Anomalies of TE performance can be observed in B1 phase under pressure.

sharp DOS peak presented near VBM for both phases. Narrow band gap, covalent bonding and multivalley electronic band structure are all contributed to good TE performance whereas the anisotropic crystal and electronic nature of $Pnma$ phase is responsible for its direction-dependent transport properties. Energy band gap will change as temperature or pressure fluctuates. At room temperature, it can only influence the transport properties in low carrier concentration (e.g., $< 1.0 \times 10^{18}$ cm $^{-3}$); but at high temperature like 600 K, it may have non-negligible effects on TE properties for carrier concentrations up to 1.0×10^{20} cm $^{-3}$, which is related to the normal doping range. Band-gap correcting is highly recommended in the transport calculations at high temperature. The multidimensional analysis of thermoelectric properties on temperatures and carrier concentrations reveal that in the low-doping case the optimal performance occurs at 300–450

K temperature range, for mid-to-high doping cases the optimal working temperature increase to a higher range. Therefore in the conventional application situations p -type PbTe within B1 phase and n -type PbTe within $Pnma$ phase are attractive choices, their optimal doping level should be determined according to the working temperature range.

Under certain pressure, crystal and electronic structures are distorted. The band gap within B1 structure has a closure at a theoretical pressure of ~ 5.2 GPa and reopens at higher pressure while the band gap within $Pnma$ structure decreases with increasing pressure and closes at a higher pressure. In view of the pressure induced energy-band modification, pressure can offer another effective method to optimize TE performance. Under high pressure, the TE properties of n -type PbTe in NaCl structure are greatly improved, with attractive values even larger than those in the p -doping case. ZT values

for *B1* phase achieve its maximum at the middoping region, at ~ 8 GPa for *p* doping and at above 18 GPa for *n* doping. In the *Pnma* case, *ZT* values are more sensitive to doping than to pressure. The *p*-type PbTe within *Pnma* phase is not competitive to *B1* phase but the *n*-type PbTe in *Pnma* phase under low pressure has better performance than *B1* phase. These findings predict the *n*-type PbTe in *B1* structure to be an attractive TE material under high pressure.

Searching the maximum of *ZT* is a challenging work for thermoelectric material research. Because of physical reasons, it appears at present to be very difficult to increase the *ZT* value of PbTe over 1.0 and there is a long way to go from this stage. Our results offer flexible ways in choosing the optimal combination of carrier concentration, working tem-

perature, and pressure to achieve higher *ZT* performance within this material. Further experimental investigation is therefore called for to verify the predictions proposed in this work.

ACKNOWLEDGMENTS

The authors are grateful for the discussions with Hui-Qiong Wang and Ning Wei (Xiamen University). This work is supported by the Minjiang Program through Xiamen University of China, Specialized Research Fund for the Doctoral Program (SRFDP) (Grant No. 20090121120028), and the Natural Science Foundation of Fujian Province, China (Grant No. 2009J01015).

*Corresponding author; jczheng@xmu.edu.cn; jin Cheng Zheng@yahoo.com

¹F. J. DiSalvo, *Science* **285**, 703 (1999).

²G. J. Snyder and E. S. Toberer, *Nature Mater.* **7**, 105 (2008).

³J. C. Zheng, *Front. Phys. China* **3**, 269 (2008).

⁴B. Wan, C. Hu, B. Feng, Y. Xi, and X. He, *Mater. Sci. Eng., B* **163**, 57 (2009).

⁵C. Wood, *Rep. Prog. Phys.* **51**, 459 (1988).

⁶Y. Zhang, X. Ke, C. Chen, J. Yang, and P. R. C. Kent, *Phys. Rev. B* **80**, 024304 (2009).

⁷T. C. Harman, D. L. Spears, and M. J. Manfra, *J. Electron. Mater.* **25**, 1121 (1996).

⁸J. C. Caylor, K. Coonley, J. Stuart, T. Colpitts, and R. Venkatasubramanian, *Appl. Phys. Lett.* **87**, 023105 (2005).

⁹G. Tai, W. Guo, and Z. Zhang, *Cryst. Growth Des.* **8**, 2906 (2008).

¹⁰K. F. Hsu, S. Loo, F. Guo, W. Chen, J. S. Dyck, C. Uher, T. Hogan, E. K. Polychroniadis, and M. G. Kanatzidis, *Science* **303**, 818 (2004).

¹¹L. J. Wu, J. C. Zheng, J. Zhou, Q. Li, J. Yang, and Y. Zhu, *J. Appl. Phys.* **105**, 094317 (2009).

¹²J. Blair and A. C. Smith, *Phys. Rev. Lett.* **7**, 124 (1961).

¹³X. Chen, Y. Wang, T. Cui, Y. Ma, G. Zou, and T. Iitaka, *J. Chem. Phys.* **128**, 194713 (2008).

¹⁴Q. Li, Y. Li, T. Cui, Y. Wang, L. J. Zhang, Y. Xie, Y. L. Niu, Y. M. Ma, and G. T. Zou, *J. Phys.: Condens. Matter* **19**, 425224 (2007).

¹⁵K. K. Zhuravlev, *Physica B* **394**, 1 (2007).

¹⁶S. V. Streltsov, A. Y. Manakov, A. P. Vokhmyanin, S. V. Ovsyannikov, and V. V. Shchennikov, *J. Phys.: Condens. Matter* **21**, 385501 (2009).

¹⁷A. N. Mariano and K. L. Chopra, *Appl. Phys. Lett.* **10**, 282 (1967).

¹⁸Y. Wang, X. Chen, T. Cui, Y. Niu, Y. Wang, M. Wang, Y. Ma, and G. Zou, *Phys. Rev. B* **76**, 155127 (2007).

¹⁹S. V. Ovsyannikov and V. V. Shchennikov, *Phys. Status Solidi B* **241**, 3231 (2004).

²⁰G. Rousse, S. Klotz, A. M. Saitta, J. Rodriguez-Carvajal, M. I. McMahon, B. Couzinet, and M. Mezouar, *Phys. Rev. B* **71**, 224116 (2005); Y. Fujii, K. Kitamura, A. Onodera, and Y. Yamada, *Solid State Commun.* **49**, 135 (1984).

²¹V. V. Shchennikov and S. V. Ovsyannikov, *Solid State Commun.* **126**, 373 (2003).

²²J. An, A. Subedi, and D. J. Singh, *Solid State Commun.* **148**, 417 (2008).

²³S. V. Ovsyannikov and V. V. Shchennikov, *Appl. Phys. Lett.* **90**, 122103 (2007).

²⁴P. Zhu, X. Jia, H. Chen, L. Chen, W. Guo, D. Mei, B. Liu, H. Ma, G. Ren, and G. Zou, *Chem. Phys. Lett.* **359**, 89 (2002).

²⁵M. A. McGuire, A. S. Malik, and F. J. DiSalvo, *J. Alloys Compd.* **460**, 8 (2008).

²⁶P. Blaha, K. Schwarz, G. K. H. Madsen, D. Kvasnicka, and J. Luitz, *WIEN2k, An Augmented Plane Wave Plus Local Orbitals Program for Calculating Crystal Properties* (Vienna University of Technology, Austria, 2001).

²⁷P. B. Allen, in *Quantum Theory of Real Materials*, edited by J. R. Chelikowsky and S. G. Louie (Kluwer, Boston, 1996), pp. 219–250.

²⁸G. K. H. Madsen and D. J. Singh, *Comput. Phys. Commun.* **175**, 67 (2006).

²⁹X. Gonze, J. M. Beuken, R. Caracas, F. Detraux, M. Fuchs, G. M. Rignanese, L. Sindic, M. Verstraete, G. Zerah, F. Jollet, M. Torrent, A. Roy, M. Mikami, P. Ghosez, J. Y. Raty, and D. C. Allan, *Comput. Mater. Sci.* **25**, 478 (2002); X. Gonze, G. M. Rignanese, M. Verstraete, J. M. Beuken, Y. Pouillon, R. Caracas, F. Jollet, M. Torrent, G. Zerah, M. Mikami, P. Ghosez, M. Veithen, J. Y. Raty, V. Olevano, F. Bruneval, L. Reining, R. Godby, G. Onida, D. R. Hamann, and D. C. Allan, *Z. Kristallogr.* **220**, 558 (2005); the ABINIT code results from a common project of the Université Catholique de Louvain, Corning Incorporated, and other collaborators, <http://www.abinit.org>

³⁰P. Hohenberg and W. Kohn, *Phys. Rev.* **136**, B864 (1964); W. Kohn and L. J. Sham, *Phys. Rev.* **140**, A1133 (1965).

³¹X. Gonze, *Phys. Rev. B* **55**, 10337 (1997); X. Gonze and C. Lee, *ibid.* **55**, 10355 (1997).

³²S. Baroni, S. de Gironcoli, A. del Corso, and P. Giannozzi, *Rev. Mod. Phys.* **73**, 515 (2001).

³³C. Hartwigsen, S. Goedecker, and J. Hutter, *Phys. Rev. B* **58**, 3641 (1998).

³⁴H. J. Monkhorst and J. D. Pack, *Phys. Rev. B* **13**, 5188 (1976).

³⁵N. Bouad, L. Chapon, R. M. Marin-Ayral, F. Bouree-Vignerone, and J. C. Tedenac, *J. Solid State Chem.* **173**, 189 (2003).

- ³⁶J. P. Perdew, K. Burke, and M. Ernzerhof, *Phys. Rev. Lett.* **77**, 3865 (1996).
- ³⁷G. K. H. Madsen, *J. Am. Chem. Soc.* **128**, 12140 (2006).
- ³⁸E. Engel and S. H. Vosko, *Phys. Rev. B* **47**, 13164 (1993).
- ³⁹Yu. I. Ravich, B. A. Efimova, and I. A. Smirnov, *Semiconducting Lead Chalcogenides* (Plenum Press, New York, 1970), Vol. 5, p. 299; D. I. Bilc, S. D. Mahanti, and M. G. Kanatzidis, *Phys. Rev. B* **74**, 125202 (2006).
- ⁴⁰D. M. Zayachuk, *Semiconductors* **31**, 173 (1997).
- ⁴¹F. D. Murnaghan, *Proc. Natl. Acad. Sci. U.S.A.* **30**, 244 (1944).
- ⁴²I. Grinberg, N. J. Ramer, and A. M. Rappe, *Phys. Rev. B* **63**, 201102(R) (2001).
- ⁴³J.-C. Zheng, C. H. A. Huan, A. T. S. Wee, R.-Z. Wang, and Y.-M. Zheng, *J. Phys.: Condens. Matter* **11**, 927 (1999).
- ⁴⁴J.-C. Zheng, *Phys. Rev. B* **72**, 052105 (2005).
- ⁴⁵R. Dornhaus, G. Nimtz, and B. Schlicht, *Narrow-Gap Semiconductors* (Springer-Verlag, Berlin, 1985).
- ⁴⁶*Semiconductors: Group IV Elements, IV-IV and III-IV Compounds*, Landolt-Börnstein, New Series, Group III Vol. 41, Pt. A, edited by O. Madelung, U. Rössler, and M. Schulz (Springer-Verlag, Berlin, 2005).
- ⁴⁷E. A. Albanesi, C. M. I. Okoye, C. O. Rodriguez, E. L. Peltzer y Blanca, and A. G. Petukhov, *Phys. Rev. B* **61**, 16589 (2000).
- ⁴⁸M. Baleva and E. Mateeva, *Phys. Rev. B* **48**, 2659 (1993).
- ⁴⁹M. W. Oh, D. M. Wee, S. D. Park, B. S. Kim, and H. W. Lee, *Phys. Rev. B* **77**, 165119 (2008).
- ⁵⁰S. H. Wei and A. Zunger, *Phys. Rev. B* **55**, 13605 (1997).
- ⁵¹G. Nimtz and B. Schlicht, *Narrow-Gap Semiconductors* (Springer-Verlag, New York, 1985), and references therein.
- ⁵²Z. H. Levine and D. C. Allan, *Phys. Rev. Lett.* **66**, 41 (1991).
- ⁵³J. C. Zheng, H. Q. Wang, C. H. A. Huan, and A. T. S. Wee, *J. Phys.: Condens. Matter* **13**, 5295 (2001).
- ⁵⁴M. Orihashi, Y. Noda, H. T. Kaibe, and I. A. Nishida, *Mater. Trans., JIM* **39**, 672 (1998).
- ⁵⁵Y. Noda, M. Orihashi, and I. A. Nishida, *Mater. Trans., JIM* **39**, 602 (1998).
- ⁵⁶J. Martin, L. Wang, L. Chen, and G. S. Nolas, *Phys. Rev. B* **79**, 115311 (2009).
- ⁵⁷A. J. Crocker and L. M. Rogers, *Br. J. Appl. Phys.* **18**, 563 (1967); I. A. Chernik, V. I. Kaidanov, M. I. Vinogradova, and N. V. Kolomoets, *Sov. Phys. Semicond.* **2**, 645 (1968); C. J. Vineis, T. C. Harman, S. D. Calawa, M. P. Walsh, R. E. Reeder, R. Singh, and A. Shakouri, *Phys. Rev. B* **77**, 235202 (2008).
- ⁵⁸P. Zhu, Y. Imai, Y. Isoda, Y. Shinohara, X. Jia, and G. Zou, *Mater. Trans.* **46**, 761 (2005).
- ⁵⁹P. Zhu, Y. Imai, Y. Isoda, Y. Shinohara, X. Jia, and G. Zou, *J. Phys.: Condens. Matter* **17**, 7319 (2005).
- ⁶⁰H. J. Goldsmid, in *Applications of the Thermoelectricity*, edited by B. L. Worsnop (Methuen, London/Wiley, New York, 1960), p. 49.
- ⁶¹J. He, A. Gueguen, J. R. Sootsman, J. C. Zheng, L. Wu, Y. Zhu, M. G. Kanatzidis, and V. P. Dravid, *J. Am. Chem. Soc.* **131**, 17828 (2009).
- ⁶²T. C. Harman, D. L. Spears, and M. P. Walsh, *J. Electron. Mater.* **28**, L1 (1999).
- ⁶³W. Zhou, J. Zhu, D. Li, H. H. Hng, F. Y. C. Boey, J. Ma, H. Zhang, and Q. Yan, *Adv. Mater.* **21**, 3196 (2009).
- ⁶⁴H. Beyer, J. Nurnus, H. Böttner, A. Lambrecht, T. Roch, and G. Bauer, *Appl. Phys. Lett.* **80**, 1216 (2002).
- ⁶⁵J. R. Sootsman, H. Kong, C. Uher, J. J. D'Angelo, C. I. Wu, T. P. Hogan, T. Caillat, and G. Kanatzidis, *Angew. Chem., Int. Ed.* **47**, 8618 (2008).
- ⁶⁶B. A. Efimova, L. A. Kolomoets, Yu. I. Ravich, and T. S. Stavitskaya, *Sov. Phys. Semicond.* **4**, 1653 (1971); Yu. I. Ravich, B. A. Efimova, and V. I. Tamarchenko, *Phys. Status Solidi B* **43**, 453 (1971).
- ⁶⁷D. J. Singh, *Phys. Rev. B* **81**, 195217 (2010).
- ⁶⁸U. V. Waghmare, N. A. Spaldin, H. C. Kandpal, and R. Seshadri, *Phys. Rev. B* **67**, 125111 (2003).